The Prediction of Separated Turbulent Flows with the Anisotropy Invariant Reynolds Stress Model (AIRSM) of Turbulence

Jovan Jovanović* and Bettina Frohnapfel†

Institute of Fluid Mechanics, Universität. Erlangen-Nürnberg, Cauerstrasse 4, 91058 Erlangen, Germany

Center of Smart Interfaces, Technische Universität Darmstadt, Petersenstr. 32, D-64287 Darmstadt, Germany

Ibrahim Hadzić ‡

CD-adapco, Nordost Park 3-5, D-90411 Nürnberg, Germany

Antonio Delgado§

Institute of Fluid Mechanics, Universität. Erlangen-Nürnberg, Cauerstrasse 4, 91058 Erlangen, Germany

Abstract

Numerical predictions with a differential Reynolds stress closure, which explicitly takes into account possible states of turbulence on the anisotropy-invariant map, are presented. The influence of anisotropy of turbulence on the modeled terms in the governing equations for the Reynolds stresses is accounted for directly. The anisotropy invariant Reynolds stress model (AIRSM) is implemented and validated in different finite-volume codes. The standard wall-function approach is employed in order to predict complex wall-bounded flows undergoing large separation. Despite the use of simple wall functions, the model performed satisfactory in predicting these flows. The predictions of the AIRSM were also compared with existing Reynolds stress models and it was found that the present model results in improved convergence compared with other models.

*Privatdozent.

†Head of Emmy Noether Resarch Group.

‡CFD Development Engineer.

§Professor and Head.

1 Introduction

In order to quantify the anisotropy of turbulence, Lumley and Newman [1] introduced the anisotropy tensor a_{ij} and its scalar invariants II_a and III_a:

$$a_{ij} = \frac{\overline{u_i u_j}}{q^2} - \frac{1}{3}\delta_{ij} \quad \text{with} \quad \overline{u_i u_i} = q^2 \;, \quad II_a = a_{ij}\, a_{ji} \;, \quad \text{and} \quad III_a = a_{ij}\, a_{jk}\, a_{ki} \;. \tag{1}$$

The tensor a_{ij} isolates the anisotropy from all other flow properties. In isotropic turbulence a_{ij}, II_a, and III_a vanish since $\overline{u_i u_j} = 1/3\, q^2\, \delta_{ij}$. If the second invariant II_a is plotted as a function of the third invariant III_a, the so-called anisotropy invariant (AI) map of Lumley and Newman is obtained, as shown in Fig. 1.

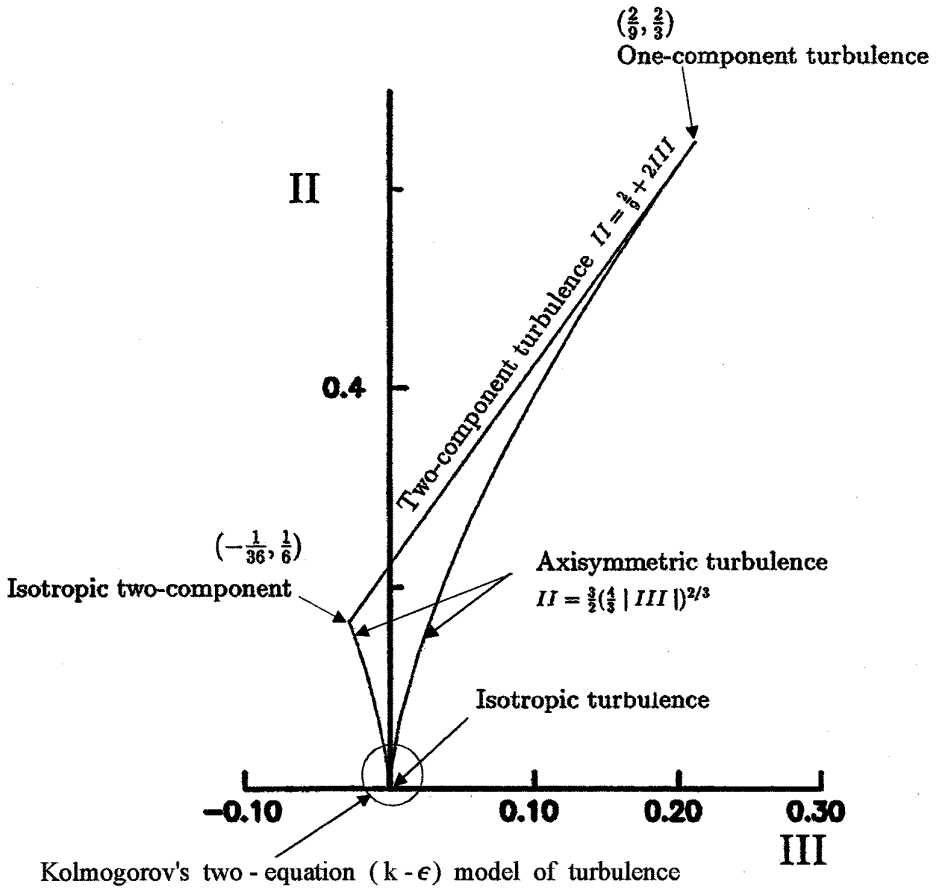

Figure 1: Anisotropy invariant map of a_{ij} and the limiting values of II_a and III_a for the different states of the turbulence. All realizable turbulence must exist within the area bounded by the map.

As found by Lumley [2], all realistic turbulence must lie within the AI map. The boundaries of the map characterize special states of turbulence. The left and right branches stand for axisymmetric turbulence. This state is reached if homogeneous isotropic turbulence is subjected to an axisymmetric contraction (left branch) or an axisymmetric expansion (right branch). The upper limit defines the two-component turbulence which is reached in the vicinity of solid walls where the wall-normal component of the fluctuations vanishes much faster than the others. Furthermore, three special points at the end of the lines surrounding the AI map are important:

the isotropic turbulence at $(0,0)$, the one-component limit $(2/9, 2/3)$ which characterizes the right limit of the map, and the limiting point on the left branch, which denotes the two-component isotropic state $(-1/36, 1/6)$.

Results of numerical simulations covering the entire map clearly support the statement of Lumley showing that nearly all states of turbulence are reached in complex turbulent flows (e.g., separated flow past an airfoil [3]). Consequently, the anisotropy of turbulence has to be taken into account when modeling turbulent flows based on statistical models to close the Reynolds-averaged Navier-Stokes equations. This issue was not systematically considered in the past and may be approached by including the influence of the limiting states in the AI map on the description of the turbulence dynamics as proposed in [4]. The basic idea is therefore to look at special states of turbulence in the AI map. Those are given by the boundaries (lines and points) mentioned above. For these special cases, turbulence closures can be found more easily than for other states of turbulence which reside within the inner region of the AI map. Under the assumption that the AI map is narrow[1], in a second step the closures for the points lying within the map are obtained by interpolation between the left, right and top boundaries and limiting states of turbulence located at the corner points of the map. In a last step, this procedure is carefully proven by a detailed comparison of the predicted results with experimental and numerical data (DNS) in order to guarantee reliability of the AI closure assumptions [4].

The present paper aims at exploiting capabilities of the above mentioned development in terms of stability, convergence and quality of results. The objective of the present work was to provide a set of flow predictions for complex flows by taking into account the anisotropy of turbulence on the AIRSM coefficients. By this way the applicability of the model equations for the treatment of a range of technically relevant flows is tested. The data predicted for selected test cases can shed light on the adequacy of representing the dynamics of complex flows based on constructions formed by interpolation of the statistical properties of turbulence which reside on the boundaries of the AI map. Keeping this in mind, we considered two test cases of separated wall-bounded flows.

2 Anisotropy Invariant Model of Turbulence

A detailed description of the AIRSM has been presented in [4]. Therefore, only an outline of the original model is presented here.

For a viscous incompressible fluid, the equations for the Reynolds stresses $\overline{u_i u_j}$ are given by

$$\frac{\partial \overline{u_i u_j}}{\partial t} + \overline{U}_k \frac{\partial}{\partial x_k}\left(\overline{u_i u_j}\right) = \underbrace{-\overline{u_i u_k}\frac{\partial \overline{U}_j}{\partial x_k} - \overline{u_i u_j}\frac{\partial \overline{U}_i}{\partial x_k}}_{P_{ij}} \underbrace{- \frac{1}{\rho}\left[\overline{u_i \frac{\partial p}{\partial x_j}} + \overline{u_j \frac{\partial p}{\partial x_i}}\right]}_{\Pi_{ij}} \tag{2}$$

$$\underbrace{-\frac{\partial}{\partial x_k}\left(\overline{u_i u_j u_k}\right)}_{T_{ij}} \underbrace{-2\,\nu \overline{\frac{\partial u_i}{\partial x_k}\frac{\partial u_j}{\partial x_k}}}_{\epsilon_{ij}} + \underbrace{\nu \frac{\partial^2 \overline{u_i u_j}}{\partial x_k \partial x_k}}_{D_{ij}}, \tag{3}$$

[1] As mentioned in [1], the AI map is narrow and therefore linear relationships between symmetric second-order correlation tensors should be more and more reliable as boundaries of the map are approached. This was demonstrated by comparisons with DNS data as shown in [4]. All DNS databases that are close to boundaries of the AI map match model approximations almost exactly.

where $\overline{U}_k$ denotes the time-averaged Cartesian velocity components and ρ and ν are the density and kinematic viscosity, respectively. The five terms on the right-hand side represent production (P_{ij}), velocity pressure-gradient interaction (Π_{ij}), turbulent transport (T_{ij}), viscous dissipation of $\overline{u_i u_j}$ (ϵ_{ij}), and viscous diffusion (D_{ij}).

To illuminate *qualitatively and not quantitatively (at all circumstances)* the dynamics of the Reynolds stresses, we utilized the closure proposals for ϵ_{ij}, Π_{ij}, and T_{ij} elaborated by Jovanović [4]. Using the two-point correlation technique and the invariant theory, he suggested the following approximations for unknown terms in the stress transport equations[2]:

$$\epsilon_{ij} \simeq \underbrace{\frac{1}{4}\nu\frac{\partial^2\overline{u_i u_j}}{\partial x_k \partial x_k}}_{\text{inhomogeneous}} + \underbrace{\mathcal{A}\, a_{ij}\, \epsilon_h}_{\text{anisotropic}} + \underbrace{\frac{1}{3}\,\epsilon_h\,\delta_{ij}}_{\text{isotropic}}\,, \tag{4}$$

$$\Pi_{ij} \simeq \underbrace{\mathcal{C}\epsilon_h a_{ij}}_{\substack{\text{non-linear part of}\\ \text{Poisson eqn.}}} + \underbrace{a_{ij}P_{ss} + \mathcal{F}\left(\frac{1}{3}P_{ss}\delta_{ij} - P_{ij}\right)}_{\substack{\text{linear part of}\\ \text{Poisson eqn.}}} + \text{small transport terms ignored}, \tag{5}$$

$$T_{ij} \approx C_s \frac{\partial}{\partial x_k}\left(\frac{k^2}{\epsilon_h}\frac{\partial\overline{u_i u_j}}{\partial x_k}\right)\,, \tag{6}$$

where $\mathcal{A}$, $\mathcal{C}$ and $\mathcal{F}$ are the scalar functions that depend on the anisotropy invariants of the Reynolds stresses ($\mathrm{II_a}$ and $\mathrm{III_a}$) and the turbulent Reynolds number R_λ (to be defined later) and the model constant C_s was fixed at 0.1.. The homogeneous part of the turbulent dissipation rate ϵ_h is defined as follows [4]:

$$\epsilon = \frac{1}{4}\nu\frac{\partial^2 q^2}{\partial x_k \partial x_k} \;+\; \epsilon_h\,. \tag{7}$$

The first term on the right-hand side of eq. (4) represents the contribution of inhomogeneity to ϵ_{ij} and the second term accounts for the influence of the anisotropy of turbulence on partition of the dissipation tensor into its components. The proposed form for ϵ_{ij} was obtained using the two-point correlation technique and satisfies the isotropy, the axisymmetry, and the two-component limit and therefore realizability. Thus it matches the well established behavior of turbulence properties for very small Reynolds numbers. The construction for $\mathcal{A}$ [see eq. (9)] was obtained by interpolation between the well established values for $\mathcal{A}$ defined at the limiting states of turbulence on the AI map. The proposed form of $\mathcal{A}$ suggests that the anisotropy in the small-scale structure of turbulence will persist even at very high Reynolds numbers.

The influence of non-linearity in the Poisson equation for the pressure fluctuations on the intercomponent energy transfer Π_{ij} is represented by the first term on the right-hand side of eq. (5). The second and third terms involved in eq. (5) originate from the linear part of the above mentioned equation for the pressure fluctuations. They are composed, with the help of the invariant function $\mathcal{F}$ [eq. (10)], to satisfy the two-component limit ($\mathcal{F} = 1$) and to match the exact expression for Π_{ij} in the rapid distortion limit and for the vanishing anisotropy of turbulence ($\mathcal{F} = 3/5$).

The approximation (6) for the turbulent transport terms T_{ij} is only provisional since it does not recognize the non-Gaussian character of turbulence at large scales and assumes that the fluctuating velocity field is weakly inhomogeneous.

[2] In the text to follow the equality sign = is used exclusively for exact relations and symbols $\simeq$ and $\approx$ imply increasing uncertainty of the relations, respectively.

The proposed forms for ϵ_{ij}, Π_{ij} and T_{ij} are the most simple constructions that are possible to arrange. Direct testing of the above suggested closures against DNS results for homogeneous turbulence and for wall-bounded and free-shear flows show overall good degree of agreement and in particular closely match to the simulated results for flows evolving at or close to the boundaries of the AI map [4].

With the the closure proposals, the transport equations for the Reynolds stresses can be written as follows:

$$\frac{\partial \overline{u_i u_j}}{\partial t} + \overline{U}_k \frac{\partial}{\partial x_k}\left(\overline{u_i u_j}\right) \simeq \underbrace{-\overline{u_i u_k}\frac{\partial \overline{U}_j}{\partial x_k} - \overline{u_j u_k}\frac{\partial \overline{U}_i}{\partial x_k}}_{P_{ij}} + a_{ij} P_{ss} + \mathcal{F}\left(\frac{1}{3} P_{ss}\delta_{ij} - P_{ij}\right)$$
$$+(\mathcal{C} - 2\mathcal{A})\epsilon_h a_{ij} - \frac{2}{3}\epsilon_h \delta_{ij} + C_s \frac{\partial}{\partial x_k}\left(\frac{k^2}{\epsilon_h}\frac{\partial \overline{u_i u_j}}{\partial x_k}\right) + \frac{1}{2}\nu \frac{\partial^2 \overline{u_i u_j}}{\partial x_k \partial x_k}\,, \tag{8}$$

where the invariant functions are defined as

$$\mathcal{A} \simeq 1 + \frac{1}{2}\left\{1 - 9\left(\frac{1}{2}\mathrm{II_a} - \mathrm{III_a}\right)\right\}(\mathcal{W} - 1) \simeq 1 + \frac{1}{2}\mathcal{J}(\mathcal{W} - 1)\,, \tag{9}$$

$$\mathcal{F} \simeq \frac{3}{5} + \frac{18}{5}\left(\frac{1}{2}\mathrm{II_a} - \mathrm{III_a}\right) \simeq 1 - \frac{2}{5}\mathcal{J}\,, \tag{10}$$

$$\mathcal{C} \simeq 4.78\left[1 - 9\left(\frac{1}{2}\mathrm{II_a} - \mathrm{III_a}\right)\right](\mathcal{W} - 1) \simeq 4.78\mathcal{J}(\mathcal{W} - 1) \tag{11}$$

$$\frac{\lambda}{L_f} \simeq -0.049 R_\lambda + \frac{1}{2}(0.009604\, R_\lambda^2 + 10.208)^{1/2}, \;\; \mathcal{W} \simeq 0.626\frac{\lambda}{L_f} \tag{12}$$

and $R_\lambda = q\lambda/\nu$ is the turbulent Reynolds number based on $q^2 = \overline{u_s u_s} = 2k$ and the Taylor microscale λ, which is related to ϵ_h as

$$\epsilon_h = 5\nu\frac{q^2}{\lambda^2}\,. \tag{13}$$

To complement the system of modeled equations for the Reynolds stresses, the following approximate form of the transport equation for ϵ_h was utilized:

$$\frac{\partial \epsilon_h}{\partial t} + \overline{U}_k \frac{\partial \epsilon_h}{\partial x_k} \simeq -2\mathcal{A}\frac{\epsilon_h \overline{u_i u_k}}{k}\frac{\partial \overline{U}_i}{\partial x_k} - \psi\frac{\epsilon_h^2}{k} + c_\epsilon \frac{\partial}{\partial x_k}\left(\frac{k^2}{\epsilon_h}\frac{\partial \epsilon_h}{\partial x_k}\right) + \frac{1}{2}\nu\frac{\partial^2 \epsilon_h}{\partial x_k \partial x_k}\,, \tag{14}$$

based on the application of the two-point correlation technique and the invariant theory [4]. To provide a robust performance of the model in predictions of complex flows, a simplified model for the decay term ψ was employed:

$$\psi \approx \psi_{2\mathrm{C}}(1 - \mathcal{J}) + \psi_{\mathrm{iso}}\mathcal{J}\,, \tag{15}$$

where $\psi_{2C} \simeq 2$ corresponds to the two-component turbulence, $\psi_{\mathrm{iso}} \simeq 1.8 - 0.4\mathcal{W}$ to isotropic grid generated turbulence, and $c_\epsilon \simeq 0.09$ was fixed to satisfy the equilibrium region in wall-bounded flows ($P_k = P_{ss}/2 \simeq \epsilon_h$).

3 Implementation of AIRSM

From the model description provided in the previous section, it can be seen that the closure formulations for the unknowns (redistribution and dissipation terms) are simpler than for other

existing models, e.g., those of Speziale et al. [8] (SSG) and Launder et al. [9] (LRR) having in mind that the influence of the limiting states on the dynamics of turbulent stresses have been taken into account even for the region around the point of vanishing anisotropy on the AI map. As a result, the numerical implementation of the model is straightforward. Unlike most other Reynolds stress models where the coefficients of the modeled terms are constant, the novel model applies scalar functions whose values are determined depending on the location of turbulence within the invariant map during the course of iterative calculations of the transport equations. In the present formulation, these scalar functions ($\mathcal{J}$, $\mathcal{F}$, etc.) are defined in terms of the unknown Reynolds stress tensor and the dissipation rate. Therefore, the difficulty in solving the coupled set of equations for mean and turbulent quantities increases. The difficulty can be overcome if the implementation of the right-hand side terms in the transport equations (8) and (14) is carried out carefully. Being implicit source terms, they can be linearized in order to enhance numerical robustness and convergence rate. The invariant scalar functions are determined from the values of the anisotropy tensor of the previous iteration. Numerically produced unphysical values of the invariant functions, especially for $\mathcal{J}$ and $\mathcal{W}$, easily caused the numerical solvers to diverge. Therefore, in order to have a robust working model, it was ensured that for both of the above-mentioned scalar functions, their numerical values remain within the bounds 0 to 1. By controlling the values of the invariant functions, it was observed that the turbulence remained within the invariant map and was not influenced by unphysical values of the Reynolds stresses or dissipation rate at some nodes during the iterative procedure. In other words, if the invariant functions are not controlled at every iteration, turbulence can easily leave the bounds of the invariant map and there is no way to bring it back into the map again.

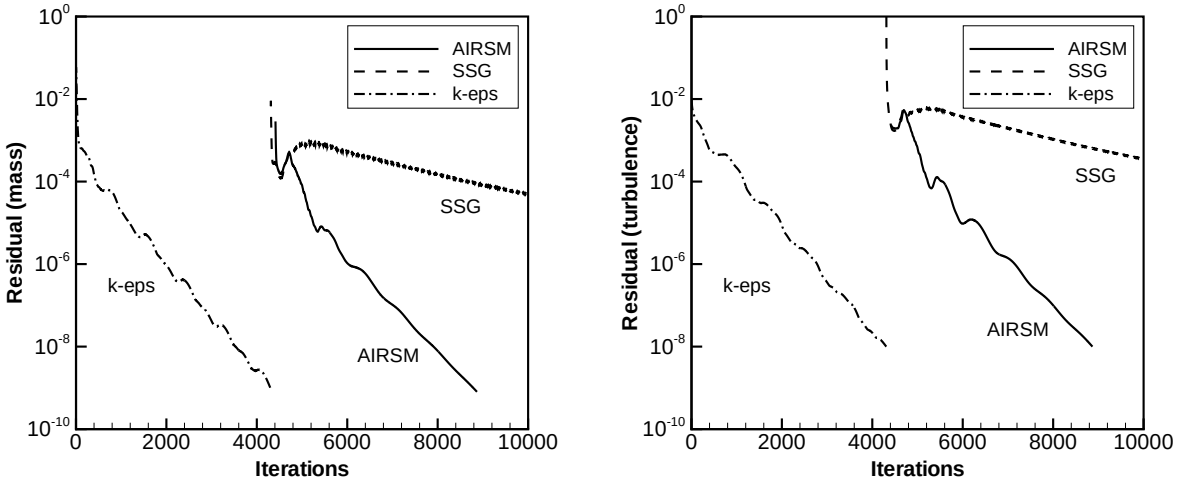

Figure 2: Comparison of convergence rates between the SSG and AIRSM models for the case of the flow over the NACA 4412 airfoil; **(a)** mass; **(b)** kinetic energy of turbulence.

In the dissipation equation, the behavior of the invariant function, i.e. ψ, is crucial. It has been shown [4] that ψ has different values at each limiting state of turbulence. This makes the formation of ψ difficult. The original model formulation when adopted in the numerical simulation, caused the computation results to be very sensitive to numerical disturbances. Therefore, for ψ a simpler model than in [4] was proposed as indicated by eq. (15).

From the basic verification simulations, it has been found that the simplified version of the model is numerically robust. The convergence rate especially on structured grids was observed to satisfy requirements for routine engineering calculations in complex geometries such as found in internal configurations of car engines. A comparison of the convergence rates for the novel model and the SSG model for the case of the flow over the NACA 4412 airfoil is shown in Fig. 2. It can be seen that despite the strong non-linearity in the closure proposals (since the scalar functions depend on the unknowns), the convergence rate of the novel model is very satisfactory.

The AIRSM model has been implemented into the in-house code FASTEST-3D [10] and the commercial codes ANSYS-CFX and CD-adapco-COMET. The standard log-law approach for walls is utilized to abridge the mean bulk flow and the no-slip wall. For the dissipation equation, the equilibrium condition, i.e. $P_k \simeq \epsilon_h$, is adopted at the wall. For the Reynolds stresses, a simple zero-gradient wall-function approach, as described by Grotjans [11], is employed. This simplified wall treatment, which prescribes that the stress gradients at the solid boundaries are set to zero in the normal-to-the-wall direction, is very convenient for routine engineering calculations of complex wall-bounded flows. However, it has to be mentioned that this boundary condition is unable to predict the high anisotropy of the stress components in the near-wall region very close to the wall. Regarding the integration down to the wall, we refer to [12, 13, 14, 15, 16].

By applying the above wall-function approach, two different problems of wall-bounded flows are taken into account. Two standard cases of separated flows, i.e. the flow in an asymmetric diffuser and past a backward-facing step, are computed. Obi et al. [18] carried out experiments for the case of an asymmetric diffuser. This case is fairly reliable since Obi et al.'s data [18] were reproduced and extended by Buice and Eaton [19].

4 Verification of AIRSM

4.1 Asymmetric Diffuser Flow

The turbulent flow in a planar diffuser is a challenging problem since it involves a wide variety of spatial scales and adverse pressure gradients. Detailed experimental investigations for a planar diffuser, with the help of a single-component laser Doppler anemometer, were performed by Obi et al. [18]. As mentioned earlier, Buice and Eaton [19] repeated the experiment in an identical configuration with the help of hot wires and pulsed wires. Adopting the RANS approach, among others Durbin [21], Iaccarino [22], and Apsley and Leschziner [23] computed the flow and turbulent stresses. Recently, Kaltenbach et al. [24] and Schlüter et al. [25] performed detailed LES computations in the same configuration. A schematic view of the computational domain for the plane asymmetric diffuser is presented in Fig. 3. The diffuser length is $21H$, where H is the inlet height. The expansion ratio of the diffuser is 4.7 and it has a single-sided deflection wall of 10°. Based on the inlet height and mean flow velocity (U_0), the Reynolds number $Re = U_0 H/\nu$ is equal to 2.12×10^4. In the governing equations, the fluid velocity and the position are normalized with respect to U_0 and H. In order to obtain appropriate flow conditions at the inlet boundary of the diffuser (at $x_1/H = -11$), a fully developed 1D channel flow computation needs to be performed. From the results of this 1D computation, the data ($\overline{U_1}$, $\overline{u_1u_1}$, $\overline{u_2u_2}$, $\overline{u_3u_3}$, $\overline{u_1u_2}$, ϵ) are interpolated on the inlet boundary of the 2D mesh. At $x_1/H = 60$, the outflow boundary with zero gradient of all variables is prescribed. At the lower, upper and inclined walls of the diffuser, the log-law of the wall is applied for the

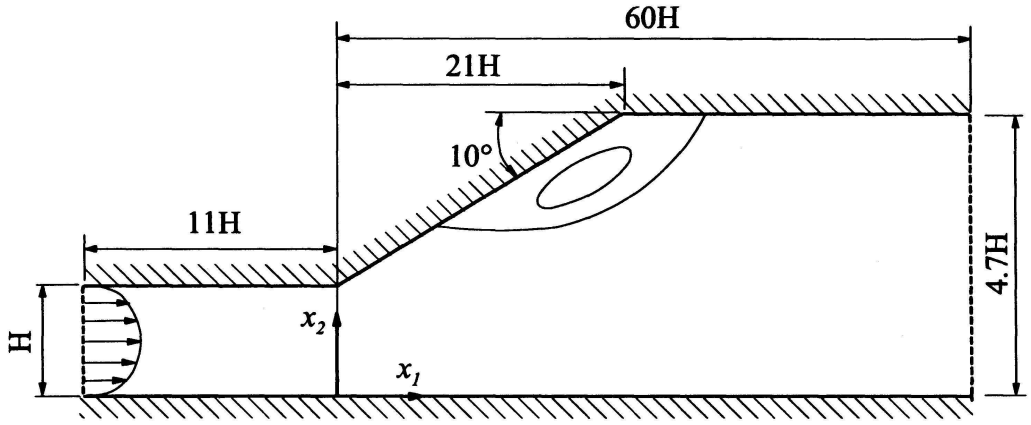

Figure 3: Schematic view of the plane 2D asymmetric diffuser.

momentum boundary condition. The numerical grid consists of 292 and 96 control volumes in the x_1 and x_2 directions, respectively. The numerical grid is substantially refined near the lower and upper walls and the region of recirculation. The present grid is considered to be sufficiently fine since the results on a one-level coarser grid were nearly the same as those of the present grid. Therefore, no attempts have been made to compute the present case on the next finer grid level.

Figure 4(a) presents the predicted streamwise velocity profiles at different stations in the region of separation. In the core region both the AIRSM and SSG models accurately predict the mean streamwise velocity. From distributions of the Reynolds stresses shown in Fig. 4(b)–(d), it can be seen that near the throat of the diffuser turbulence changes rapidly. Away from the near-wall region, both the SSG and AIRSM models capture trends in the experimental results reasonably, both for the normal and shear stresses. It can be noted that further downstream in the throat ($x_1/H > 15$), the prediction of turbulent stresses based on the AIRSM model are slightly better than those of the SSG model.

From the skin-friction coefficients C_f for both the bottom and inclined walls of the diffuser, as shown in Fig. 5, it can be seen that all the models deviate from the experimentally measured values of C_f. It is a well-known fact that the wall functions are responsible for the underprediction of the skin-friction coefficient (see, e.g. [21]). In the separation region, the AIRSM model predicts the flow field slightly better than the SSG model, but the differences between both models are much smaller than the deviations to the experimental data. In the case of the k-ϵ model, the separation region is not predicted at all.

4.2 Backward-Facing Step Flow

The turbulent flow over a backward-facing step (see Fig. 6) is a widely used benchmark problem to evaluate the performance of turbulence models for separated flows, because the geometry of the test case is simple and the separation occurs at the sharp corner. Hence the flow is easier to predict than a flow for which the separation point is unknown. Moreover, both DNS and LES data for this flow problem are commonly available in the literature. The present case is based on the experiment of Driver and Seegmiller [26]. The dimensions of the computational domain are shown in Fig. 6, where $H = 0.0127$ m. The main domain dimensions in the x_1, x_2, and x_3 directions are $30H$, $9H$, and $0.1H$, respectively. The top wall is either parallel to

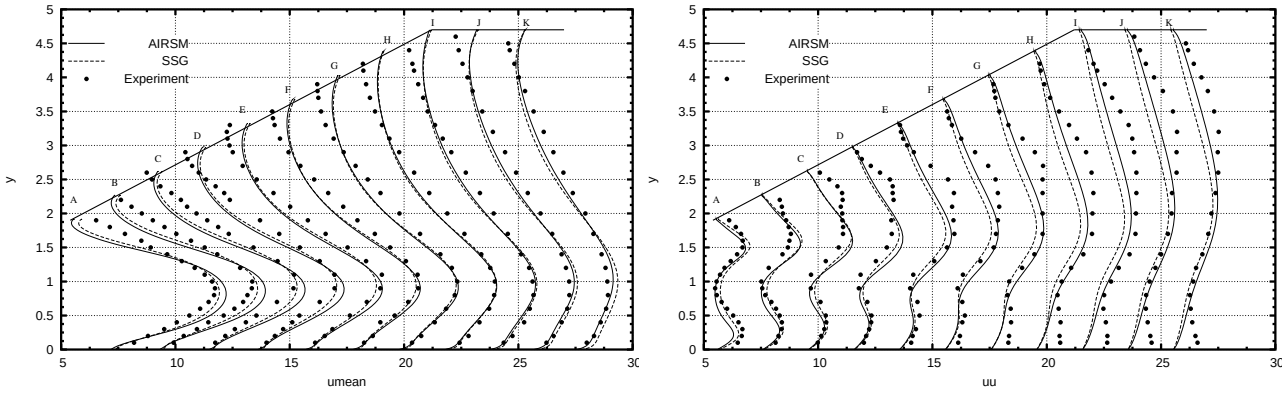

(a) $\overline{U}_1$ (b) $\overline{u_1 u_1}$

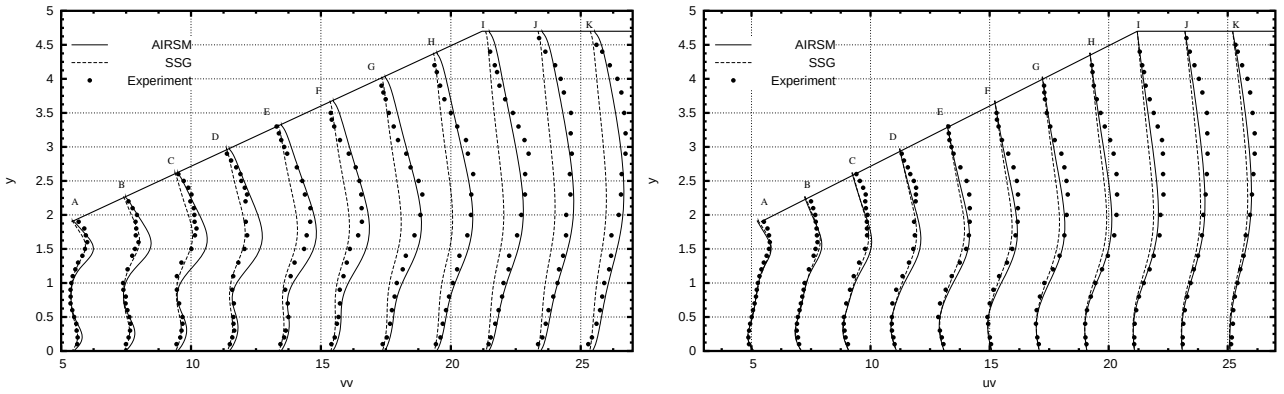

(a) $\overline{u_2 u_2}$ (b) $\overline{u_1 u_2}$

Figure 4: Comparison of (a) predicted mean flow, $\overline{U_1}$, and (b)–(d) Reynolds stress components at different stations ($x_1/H = 5.2$–25.2) with the measurements of Obi et al. [18] in an asymmetric 2D diffuser.

the bottom wall along which separation develops or is diverging at 6 degrees starting at the point opposite to the step. The flow is computed in a two-dimensional manner using a 3-D code. The kinematic viscosity ν is equal to 1.5×10^{-5} m^2/s. Based on the centerline velocity, $U_{ref} = 44.2$ m/s at the inlet, and the step height H, the Reynolds number is $Re_H = 3.75 \times 10^4$. Inlet profiles for velocities and turbulence quantities are obtained from preliminary calculations of the flow development in a plane channel of the height H by varying flow conditions at the channel entrance until the outlet results matched the experimental data for the mean flow and turbulence statistics at four step heights ($4H$) upstream of the step corner.

Similar to the case of the diffuser, the normal-to-the-wall gradients of the Reynolds stresses are set to zero at the lower and upper walls of the step. For the momentum boundary condition at the wall, the logarithmic law is taken into account. The outlet condition is applied 30 step heights ($30H$) downstream of the step.

For both cases, i.e. $\alpha = 0°$ and $\alpha = 6°$, a coarse (see Fig. 7) and a fine grid were generated to check grid independence. The number of grid points are about 4600 and 9600, respectively. As depicted in Fig. 7, the grid is locally refined in the region around the step and especially in the region of the free shear layer.

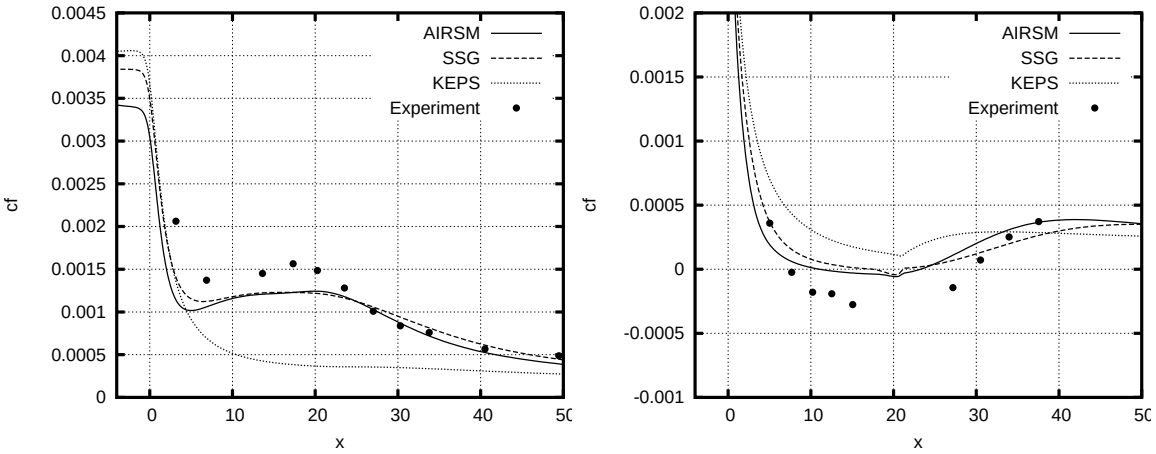

Figure 5: Distribution of the skin-friction coefficient $C_f = \tau_w/(\frac{1}{2}\rho U_0^2)$ for the case of an asymmetric diffuser; (a) bottom wall; (b) inclined wall.

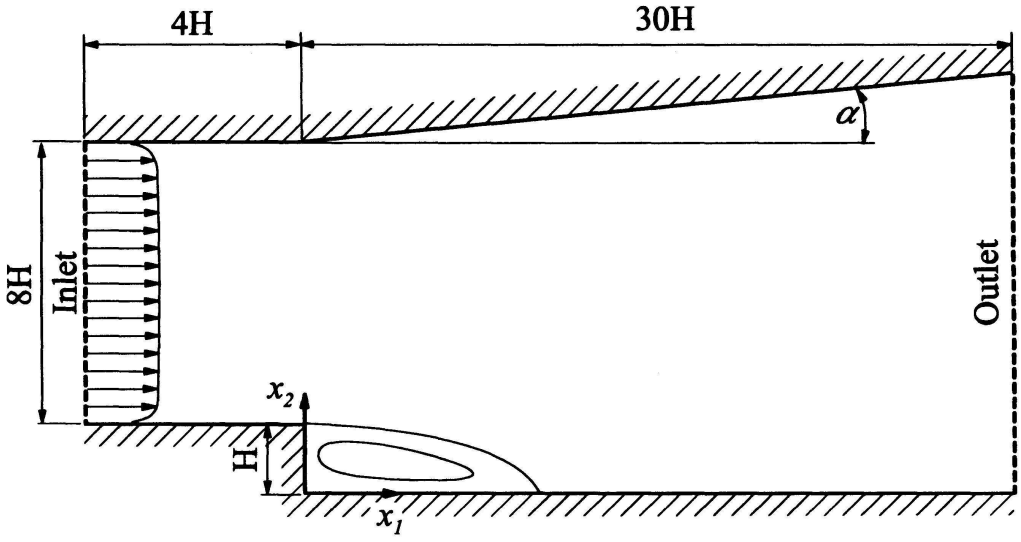

Figure 6: Description of the backward-facing step test case. The experiment was performed by Driver and Seegmiller [26].

In the present case, the computations were performed with the k-ϵ, SSG and AIRSM models. As mentioned above, the computations were carried out on two different grids. It was observed that the results on the coarse grid are not significantly different from those on the finer grid (which is about two times finer in the x_1-x_2 plane). Hence, in the present section only fine grid results are presented.

First, the mean flow is investigated by plotting the streamlines in the region where the step is located. From the streamlines shown in Fig. 8, it can be observed that the reattachment lengths predicted by the k-ϵ model ($5.29H$ for $\alpha = 0°$ and $6.5H$ for $\alpha = 6°$) are significantly smaller than the experimentally obtained values of $6.26H$ and $8.30H$ for $\alpha = 0°$ and $\alpha = 6°$, respectively. On the other hand, the predicted reattachment lengths obtained by the SSG

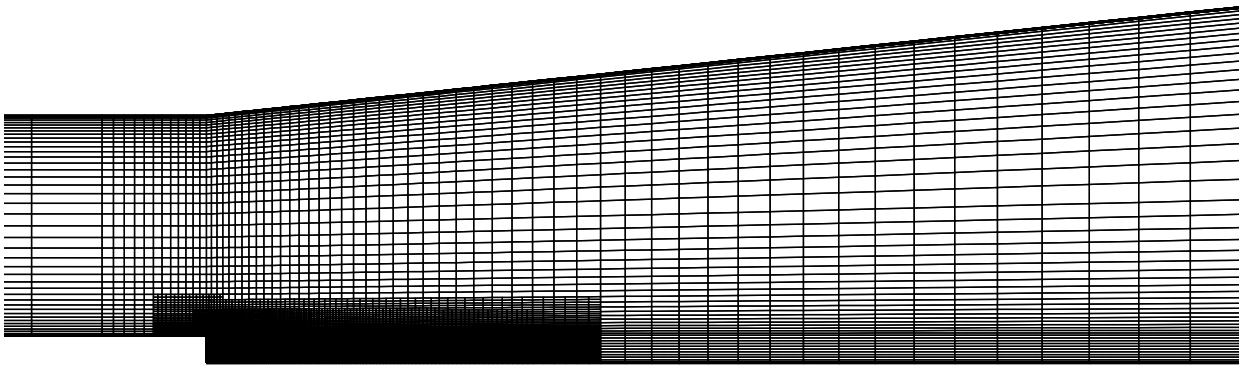

Figure 7: Coarse numerical grid and local grid refinement used for the flow over a backward-facing step at $\alpha = 6°$.

model are approximately equal to $5.54H$ for $\alpha = 0°$ and $6.63H$ for $\alpha = 6°$ and thus slightly in better agreement with the experimental values than those of the k-ϵ model. This outcome is consistent with the literature stating that the SSG model acts towards the shortening of the recirculation zone. Applying the AIRSM model the reattachment lengths are equal to $5.9H$ for $\alpha = 0°$ and $7.42H$ for $\alpha = 6°$. Thus, in comparison with the SSG model the deviations to the experiment are approximately halved by the AIRSM model for both configurations. Furthermore, a secondary vortex is visible in the corner past the step for the AIRSM and the SSG model but not for the k-ϵ model results.

Another noteworthy feature concerns the back-bending of the mean dividing streamline at reattachment, which is a traditional outcome of existing Reynolds stress models, see e.g. Lasher and Taulbee [27] and Hanjalić and Jakirlic [28]. As visible in Figs. 8(e) and (f), the predictions using the novel model does not show this deficiency.

Detailed velocity profiles at various locations (x_1/H) behind the step are depicted in Fig. 9. Away from the near-wall region both the SSG and AIRSM models satisfactorily predict the mean flow. By carefully observing the region close to the wall in Fig. 9, one can see that the prediction of the AIRSM model at some locations is in slightly better agreement with the experimental results than the results obtained by the SSG model, but the deviations are small.

Furthermore, two important parameters, C_f and C_P, are determined in order to characterize the flow separation and reattachment. The pressure coefficient is defined as

$$C_P = \frac{P - P_0}{\frac{1}{2}\rho U_{ref}^2}, \tag{16}$$

where P_0 corresponds to the reference pressure at $4H$ before the step. Hence these two coefficients are predicted from the step onwards and plotted in Fig. 10. From these two plots, one can infer that both AIRSM and SSG models broadly follow the trends in the experimental data in character and magnitude but not over the details.

In Figs. 11 and 12 the longitudinal, normal, and shear stresses are plotted in order to estimate the performance of the AIRSM and SSG models. Despite the use of simple wall

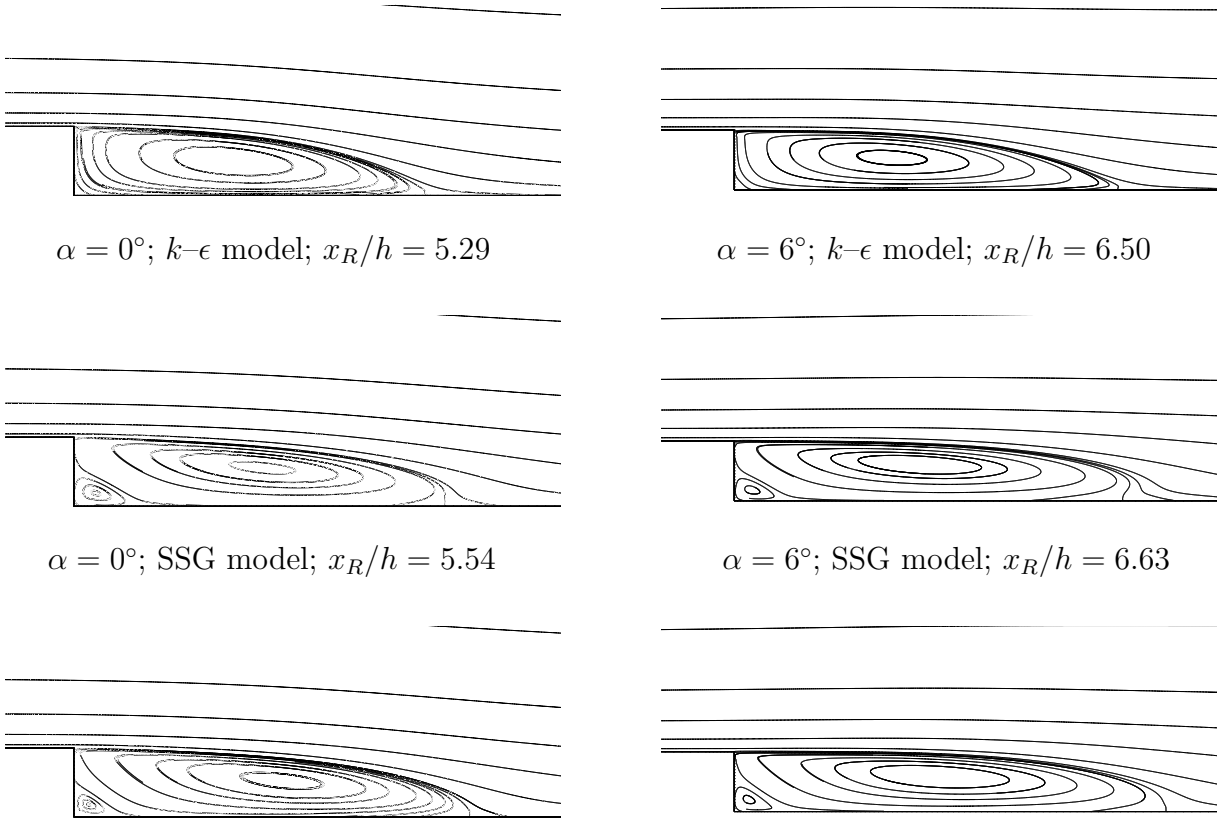

$\alpha = 0°$; k–ϵ model; $x_R/h = 5.29$ | $\alpha = 6°$; k–ϵ model; $x_R/h = 6.50$

$\alpha = 0°$; SSG model; $x_R/h = 5.54$ | $\alpha = 6°$; SSG model; $x_R/h = 6.63$

$\alpha = 0°$; AIRSM model; $x_R/h = 5.90$ | $\alpha = 6°$; AIRSM model; $x_R/h = 7.42$

Figure 8: Streamlines predicted by different turbulence models in case of the flow over the backward-facing step with the wall opposite to the step parallel to the wall (left) or diverging at $\alpha = 6°$ (right).

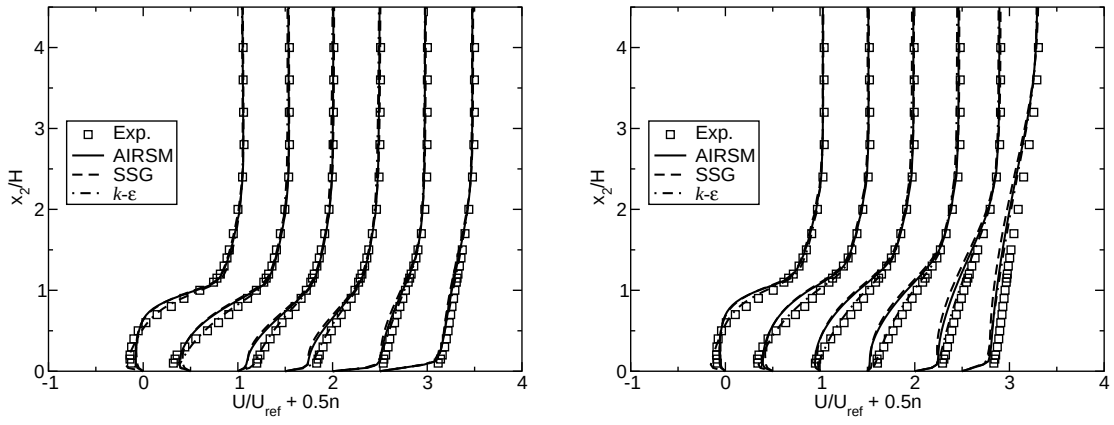

$\alpha = 0°$ | $\alpha = 6°$

Figure 9: Velocity profiles at stations $x_1/H = 2$, 4, 6.5, 8, 14, 32. From left to right, $n = 0$, 1, 2, 3, 4 and 5; experimental data by Driver and Seegmiller [26].

functions for the Reynolds stresses and the restrictive formulation of the AIRSM model, it can be seen that the agreement of the experimental results with the numerical predictions

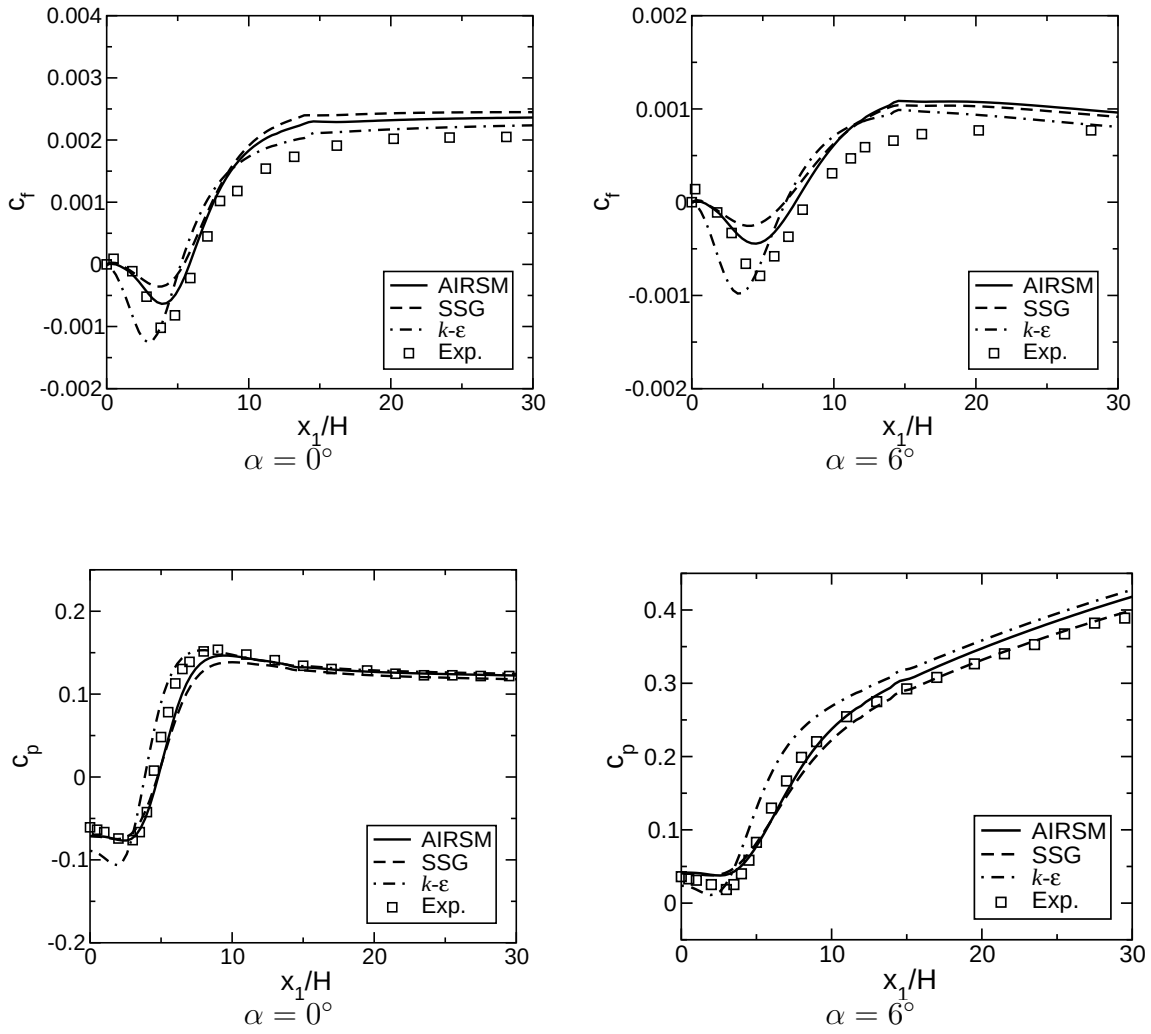

Figure 10: Distributions of the skin-friction coefficient and the pressure coefficient predicted by different turbulence models for the backward-facing step flow; experimental data by Driver and Seegmiller [26].

based on both models considered are reasonable. However, a closer look at the results near the step corner suggest that predictions obtained with the aid of the AIRSM model match more closely the experimental data than the predictions obtained with the SSG model. These small differences are for example visible in the profiles of the streamwise component of the Reynolds stress tensor shown on top of Figs. 11 and 12. Especially in the reattachment and post-reattachment regions both models overpredict the normal stress component $\overline{u_1 u_1}$, but for AIRSM the agreement with the measurements is slightly better than for the SSG model.

5 Conclusion

Numerical predictions of complex turbulent wall-bounded flows were carried out using the novel Reynolds stress turbulence model based on the application of the two-point correlation technique and invariant theory. The simplified set of the modeled equations was implemented

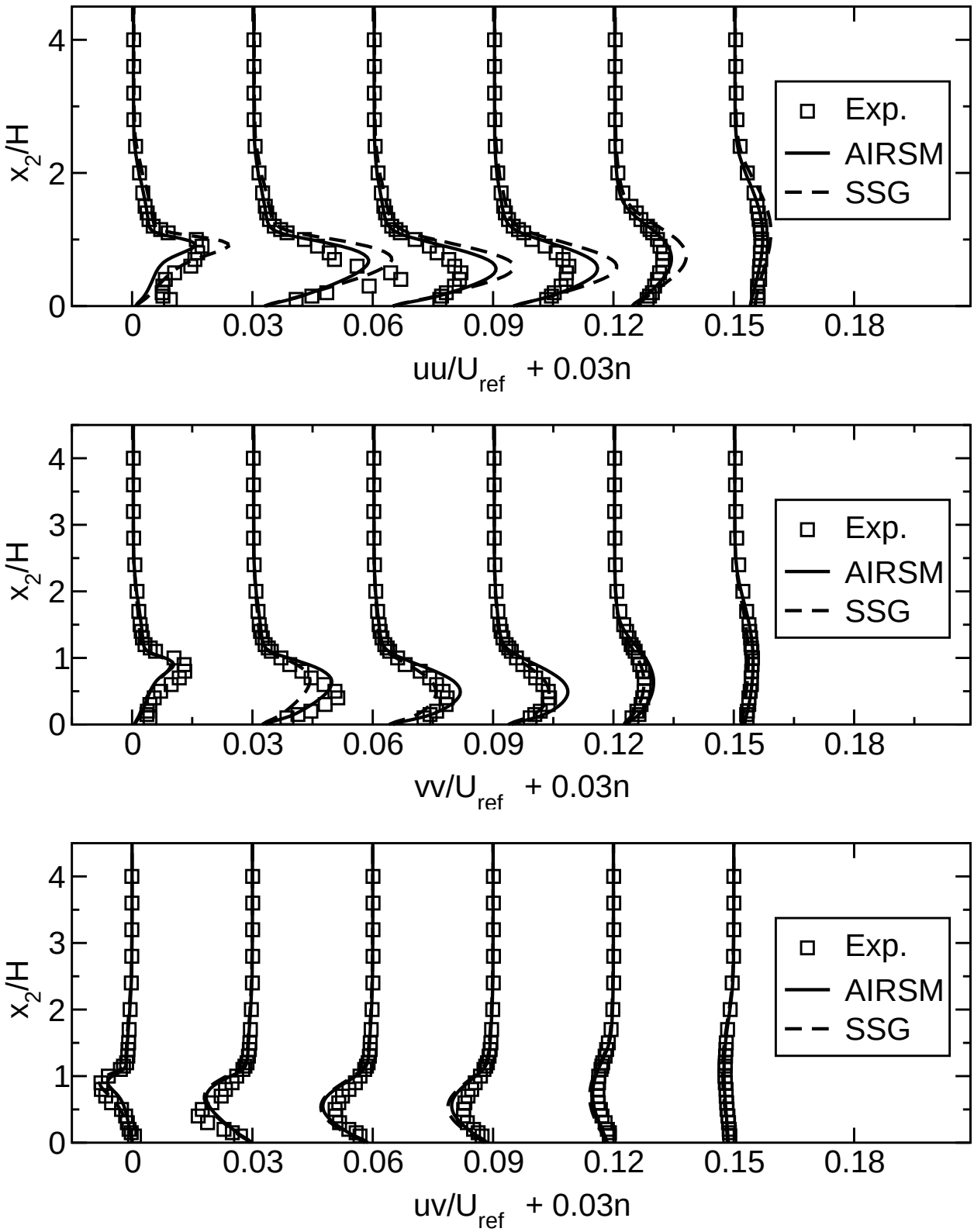

Figure 11: Reynolds stress components predicted by the AIRSM and the SSG models in the backward-facing step case at $\alpha = 0°$, Plotted data are extracted at stations $x_1/H = 2$, 4, 6.5, 8, 14, 32 and normalized with the bulk flow velocity U_{ref} at the inlet of the channel. From left to right, $n = 0$, 1, 2, 3, 4 and 5; experimental data by Driver and Seegmiller [26].

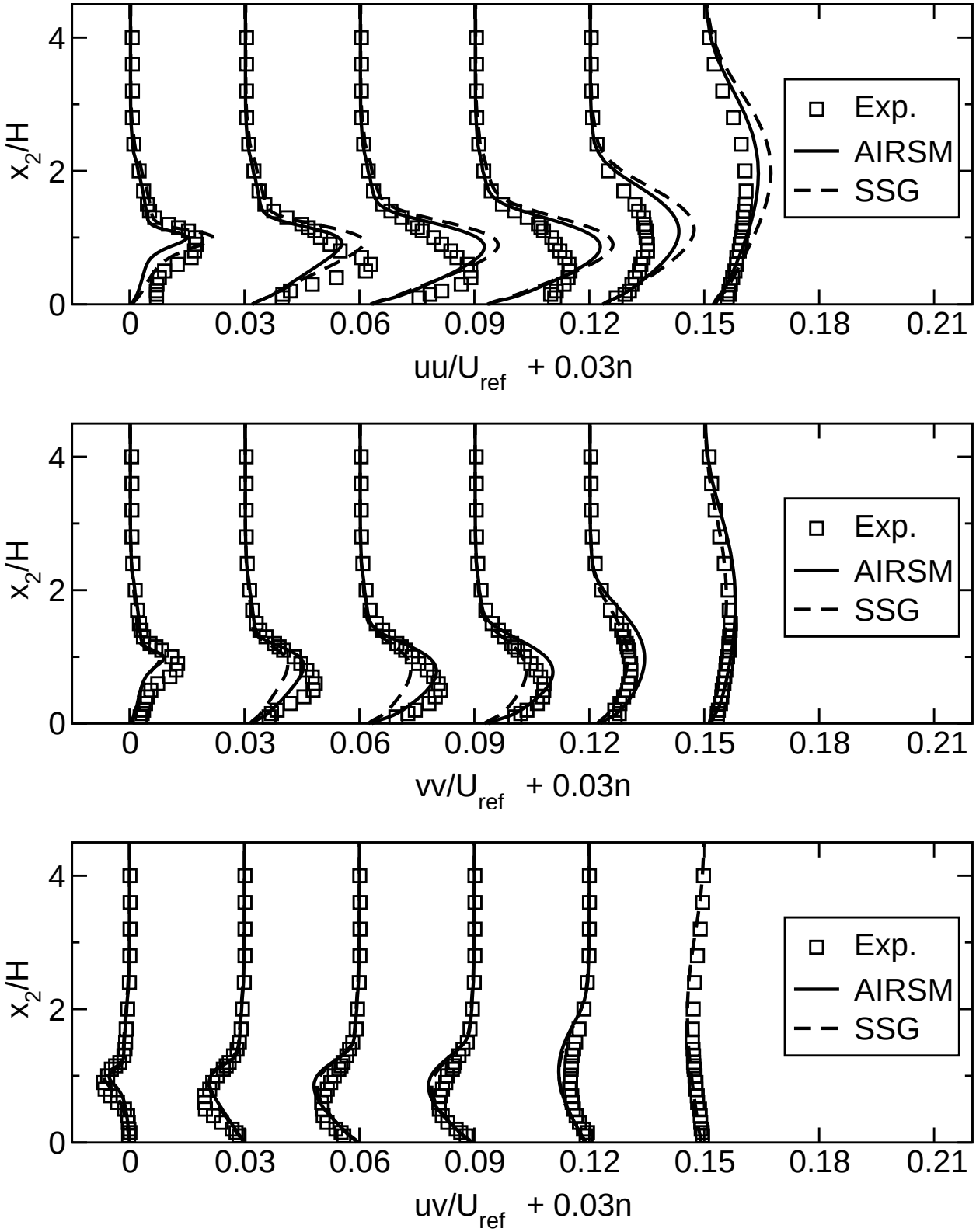

Figure 12: Reynolds stress components predicted by the AIRSM and the SSG models in the backward-facing step case at $\alpha = 6°$, Plotted data are extracted at stations $x_1/H = 2$, 4, 6.5, 8, 14, 32 and normalized with the bulk flow velocity U_{ref} at the inlet of the channel. From left to right, $n = 0$, 1, 2, 3, 4 and 5; experimental data by Driver and Seegmiller [26].

into the computer programs FASTEST-3D, ANSYS-CFX and CD-adapco-COMET. Numerical predictions were performed using the standard wall-function approach for the treatment of the flow close to solid boundaries.

Sample calculations of two standard test cases of wall-bounded flows, namely the flow developing in an asymmetric diffuser and the backward-facing step flow show improved agreement between the predicted and experimental results in comparison with the performance of concurrent turbulence closures used in engineering practice. For the case of the backward-facing step flow the predicted reattachment lengths were closer to the experimental findings than the corresponding results obtained using other models. It is interesting that the present calculations show that the turbulence properties are captured quite well in spite of the use of wall functions and follow more or less closely the trends in the experimental data across the entire flow domain. Furthermore, the convergence rates of the AIRSM model was found to be improved compared to the SSG model.

Acknowledgments

This work is supported by the Deutsche Forschungsgemeinschaft under contracts Jo 240/3-2 and Jo 240/5-1 which is gratefully acknowledged.

References

[1] J.L. Lumley and G. Newman. Return to Isotropy of Homogeneous Turbulence. *Journal of Fluid Mechanics*, 82:161–178, 1977.

[2] J.L. Lumley. Computational Modeling of Turbulent Flows. *Advances in Applied Mechanics*, 18:123–176, 1978.

[3] N. Jovičić, M. Breuer, and J. Jovanović. Anisotropy–Invariant Mapping of Turbulence in a Flow Past an Unswept Airfoil at High Angle of Attack. *J. Fluids Engineering*, 128(3):559–567, 2006.

[4] J. Jovanović. *The Statistical Dynamics of Turbulence*. Springer, 2004.

[5] C.C. Shir. A Preliminary Study of Atmospheric Turbulent Flow in the Idealized Planetary Boundary Layer. *J. Atmos. Sci.*, 30:1327–1339, 1973.

[6] M. Hällback, J. Groth, and A.V. Johansson. An Algebraic Model for Non-isotropic Turbulent Dissipation Rate in Reynolds Stress Closure. *Phys. Fluids*, A 2:1859–1866, 1990.

[7] A.N. Kolmogorov. Local Structure of Turbulence in an Incompressible Fluid at Very High Reynolds Numbers. *Dokl. Akad. Nauk SSSR*, 30:299–303, 1941.

[8] C.G. Speziale, S. Sarkar, and T.B. Gatski. Modeling of Pressure-Strain Correlation of Turbulence: An Invariant Dynamical System Approach. *Journal of Fluid Mechanics*, 227:245–272, 1991.

[9] B. E. Launder, G.J. Reece, and W. Rodi. Progress in the Development of a Reynolds-Stress Turbulence Closure. *Journal of Fluid Mechanics*, 68:537–566, 1975.

[10] F. Durst, M. Schäfer, and K. Wechsler. Efficient Simulation of Incompressible Viscous Flows on Parallel Computers. *Notes Numer. Fluid Mech.*, 52:87–101, 1996.

[11] H. Grotjans. *Turbulenzmodelle höherer Ordnung für komplexe Anwendungen.* PhD thesis, TU München, 1999.

[12] S. Jakirlic and K. Hanjalić. A New Approach to Modelling Near-Wall Turbulence Energy and Stress Dissipation. *Journal of Fluid Mechanics*, 459:139–166, 2002.

[13] R. Manceau and K. Hanjalić. Elliptic Blending Model: A New Near-Wall Reynolds-Stress Turbulence Closure. *Phys. Fluids*, 14(2):744–754, 2002.

[14] B.E. Launder and S.-P. Li. On the Elimination of Wall-Topography Parameters from Second-Moment Closure. *Phys. Fluids*, 6(2):999–1006, 1994.

[15] M. Dianat, M. Fairweather, and W.P. Jones. Reynolds Stress Closure Applied to Axisymmetric, Impinging Turbulent Jets. *Theoret. Comput. Fluid Dynamics*, 8:435–447, 1996.

[16] T.J. Craft and B.E. Launder. A Reynolds Stress Closure Designed for Complex Geometries. *Int. J. Heat Fluid Flow*, 17(3):245–254, 1996.

[17] R.D. Moser, J. Kim, and N.N. Mansour. Direct Numerical Simulation of Turbulent Channel Flow up to $Re_\tau = 590$. *Phys. Fluids*, 11:943–946, 1999.

[18] S. Obi, K. Aoki, and S. Masuda. Experimental and Computational Study of Turbulent Separated Flow in an Asymmetric Diffuser. In *Proc. 9th Symp. on Turbulent Shear Flows, Kyoto*, 1993.

[19] C.U. Buice and J.K. Eaton. Experimental Investigation of Flow Through an Asymmetric Plane Diffuser. Technical report, Center of Turbulence Research, Stanford University, 1996. CTR Annual Research Briefs.

[20] S. Ray. personal communication, 2006.

[21] P.A. Durbin. On the k-ϵ Stagnation Point Anomaly. *Int. J. Heat Fluid Flow*, 17:89–91, 1996.

[22] G. Iaccarino. Predictions of a Turbulent Separated Flow Using Commercial CFD Codes. *ASME Journal of Fluids Engineering*, 123:819–828, 2001.

[23] D.D. Apsley and M.A. Leschziner. Advanced Turbulence Modelling of Separated Flow in a Diffuser. *Journal of Flow, Turbulence and Combustion*, 63:81–112, 1999.

[24] H.J. Kaltenbach, M. Fatica, R. Mittal, T.S. Lund, and P. Moin. Study of Flow in a Planar Asymmetric Diffuser using Large-Eddy Simulation. *Journal of Fluid Mechanics*, 390:151–185, 1999.

[25] J.U. Schlüter, X. Wu, and H. Pitsch. Large-Eddy Simulation of a Separated Plane Diffuser. *AIAA Paper*, 2005.

[26] D.M. Driver and H.L. Seegmiller. Feature of a Reattachment Turbulent Shear Layer in a Divergent Channel Flow. *AIAA J.*, 23:163–171, 1985.

[27] W.C. Lasher and D.B. Taulbee. On the Computation of Turbulent Backstep Flow. *Int. J. Heat Fluid Flow*, 13(1):30–40, 1992.

[28] K. Hanjalić and S. Jakirlić. Contribution towards the Second-Moment Closure Modelling of Separating Turbulent Flows. *Computers and Fluids*, 27(2):137–156, 1998.